NEUROSCIENCE

Predictive grid coding in the medial entorhinal cortex

Ayako Ouchi[1] and Shigeyoshi Fujisawa[1,2]*

The entorhinal cortex represents allocentric spatial geometry and egocentric speed and heading information required for spatial navigation. However, it remains unclear whether it contributes to the prediction of an animal's future location. We discovered grid cells in the medial entorhinal cortex (MEC) that have grid fields representing future locations during goal-directed behavior. These predictive grid cells represented prospective spatial information by shifting their grid fields against the direction of travel. Predictive grid cells discharged at the trough phases of the hippocampal CA1 theta oscillation and, together with other types of grid cells, organized sequences of the trajectory from the current to future positions across each theta cycle. Our results suggest that the MEC provides a predictive map that supports forward planning in spatial navigation.

The cognitive map theory proposes that the brain builds an allocentric spatial representation of the environment to support the planning of future travel (*1*, *2*). Several decades of neurophysiological research suggests that cognitive maps are configured and used across the hippocampal–entorhinal cortex axis (*3*, *4*). In particular, the entorhinal cortex organizes representations of spatial geometry and self-motion information—including spatial grid, environmental boundary, head direction, and speed representations—integrating sensory and motor cues to compose allocentric spatial information then sent to the hippocampus (*5–10*). Recent theoretical and experimental studies have shown that the population activity of such medial entorhinal cortex (MEC) grid cells configures a low-dimensional continuous attractor network and that rat movement can be represented by trajectories on this manifold, allowing the updating of robust positional information (*11*, *12*). However, it remains unclear whether and how the entorhinal grid system is involved in organizing goal-directed trajectory sequences by predicting future spatial information.

Predictive grid cells in the MEC

To investigate the predictive coding properties of the MEC neurons, we designed a goal-directed behavioral task in a two-dimensional open field. Rats were required to move back and forth between the two water reward ports, whose positions were changed every 20 trials, so that the whole environment was covered with vertical, horizontal, and diagonal trajectories (Fig. 1 and fig. S1). This task consists of multiple linear tracks in each direction in the open field and was specifically designed to detect and quantify the predictive bias in the allocentric two-dimensional spatial representation of neurons. We recorded extracellular single units from layers 2 and 3 of the MEC and the CA1 of the rats during the task using high-density multishank silicon probes (Fig. 1C). To assess whether MEC neurons encode future spatial information, we constructed neuronal firing rate maps using the actual position of the rat, as well as positions shifted backward and forward along the rat's trajectory (Fig. 1D). A subset of MEC neurons showed robust grid structures in the rate map of the future projected positions, although they did not show gridness in the rate maps of the original positions (Fig. 1E and fig. S2). We calculated the gridness scores, which measure the 60° periodicity in the spatial autocorrelation of the rate map, as a function of the spatial shift relative to the original positions. The gridness scores were maximal at several tens of centimeters ahead of the actual positions. Thus, we hypothesized that these neurons predictively organize grid fields for future projected positions, and we termed these neurons predictive grid cells.

We next investigated the coding principles of the predictive grid cells. The model of the representation of predictive grid cells at current and future positions is shown in Fig. 2A. Because the predictive grid cells have the highest gridness at future projected locations, the grid fields should be shifted in the approach direction relative to the direction of travel. Therefore, a rate map that includes all directions would be averaged out and smoothed because of the overlap of the grid fields shifted in different directions. On the other hand, a rate map calculated separately for each direction would show a grid structure even at the original position. We therefore constructed a rate map in each traveling direction separately. In agreement with the model, the rate maps sorted by the running directions exhibited clear grid representations, whereas firing rate maps including all trajectories did not (Fig. 2B). The firing rate plots constructed from the linearized position in each block showed that the grid peaks were shifted in alternating patterns toward the approach direction relative to direction of travel (Fig. 2B and fig. S3A).

Because theta oscillations play a central role in information processing in the hippocampal–entorhinal cortical circuit, we examined whether and how the firing of the predictive grid cells was modulated by CA1 theta oscillations. The predictive grid cells were tightly phase-locked to the troughs (~180°) of theta oscillations referenced to the CA1 pyramidal cell layer (Fig. 2B). We also analyzed the firing properties of standard grid cells as previously reported (*5*, *13*). One group of grid cells exhibited phase precession, starting at about 180° and ending at 270° in each grid field (Fig. 2C and figs. S3B and S4A) (*13*), referred to here as "phase-precession grid cells." The other group of grid cells showed phase-locking to the peak of theta oscillations (Fig. 2D and fig. S4B) (*13*), referred to here as "phase-locked grid cells," which prefer the phase opposite to those of the predictive grid cells. Thus, the predictive, phase-precession, and phase-locked grid cells had different theta phase preferences, suggesting the differential role of temporal coding mediated by theta oscillations.
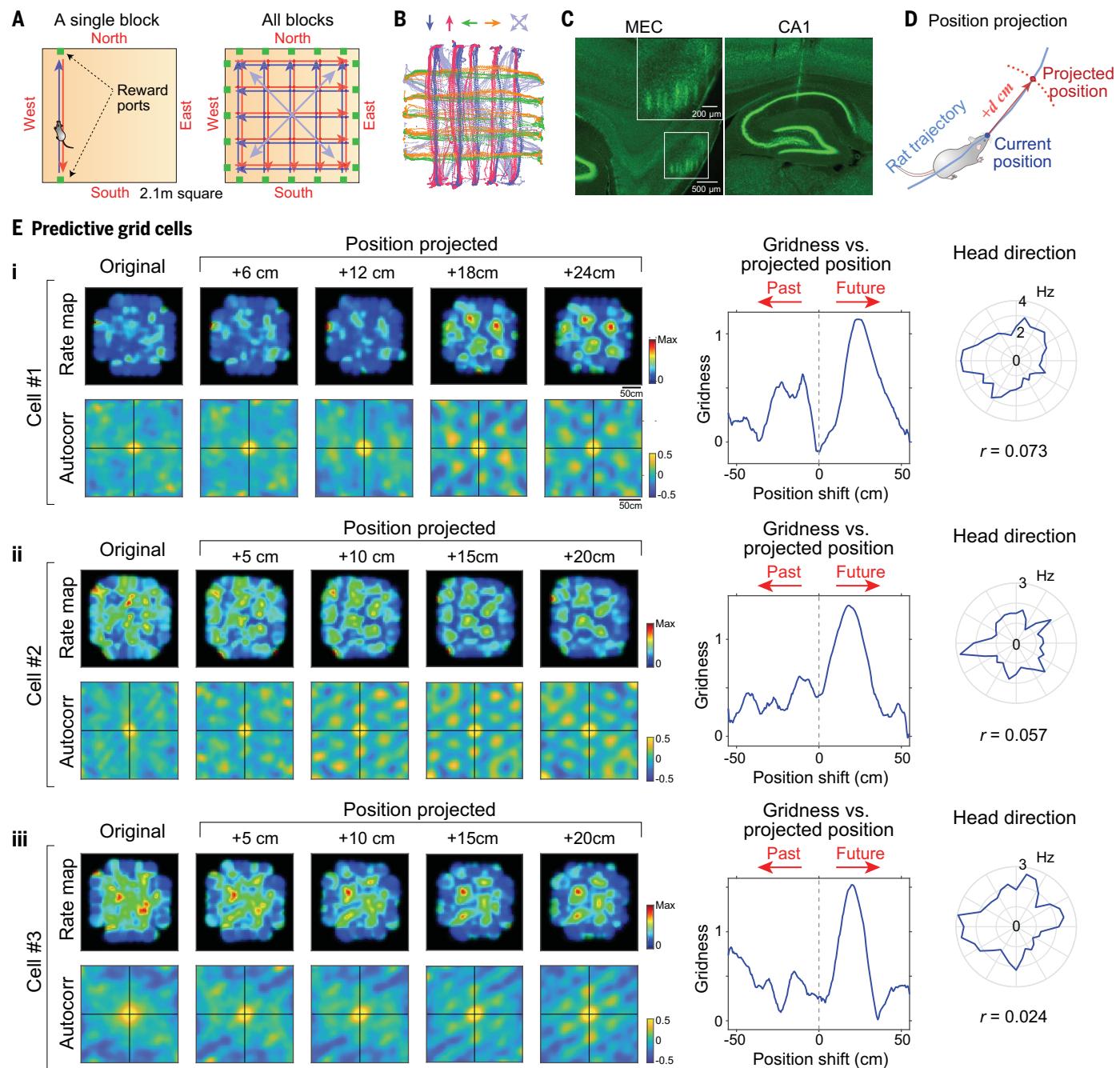
### Coding properties of predictive grid cells

To explore the coding properties of these neurons at the population level, we defined criteria for predictive grid cells as follows: (i) The gridness score of the rate map has the maximum value at a future position that is significant compared with shuffled data, whereas the gridness score at the original position is not significant, and (ii) spike times are phase-locked around 180° of CA1 theta oscillations. We also categorized grid cells as phase-precession and phase-locked grid cells in line with the previous study (*13*). Using these criteria, we identified 305 predictive grid cells, 558 phase-precession grid cells, and 241 phase-locked grid cells across six rats (Fig. 3 and table S1). The average optimal position shift of the predictive grid cells was 22.5 ± 10.2 cm (mean ± SD) (Fig. 3F), corresponding to approximately one-quarter of the grid spacing of each neuron (0.27 ± 0.11; mean ± SD) (Fig. 3G). The optimal position shift of the phase-precession grid cells was also positive, but significantly smaller than that of the predictive grid cells (4.5 ± 8.8 cm; mean ± SD) (Fig. 3F). The optimal shift of the phase-locked grid cells was close to zero (0.8 ± 9.0 cm; mean ± SD) (Fig. 3F). The optimal grid shifts of the predictive grid cells were constant regardless of the direction of travel (fig. S5). Previous studies have reported that MEC neurons are modulated by self-motion signals, including speed and head direction (*6*, *8*). We thus calculated speed modulations and found that 25.9% [Clopper-Pearson confidence intervals (CIs) for 99%, CI = 19.7 to 32.9%], 87.5% (CI = 83.4 to 90.8%), and 47.7% (CI = 39.3 to 56.2%) of the predictive, phase-precession, and

[1]Laboratory for Systems Neurophysiology, RIKEN Center for Brain Science, Wako City, Saitama 351-0198, Japan. [2]Department of Complexity Science and Engineering, The University of Tokyo, Kashiwa, Chiba 277-8561, Japan.
*Corresponding author. Email: shigeyoshi.fujisawa@riken.jp
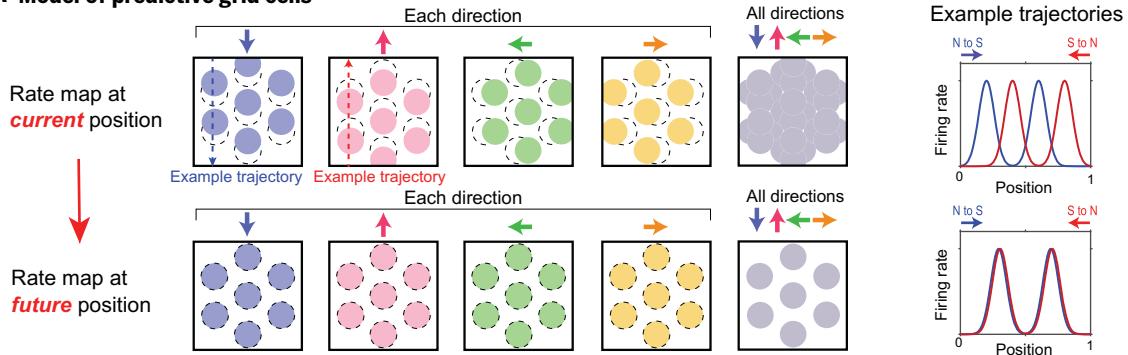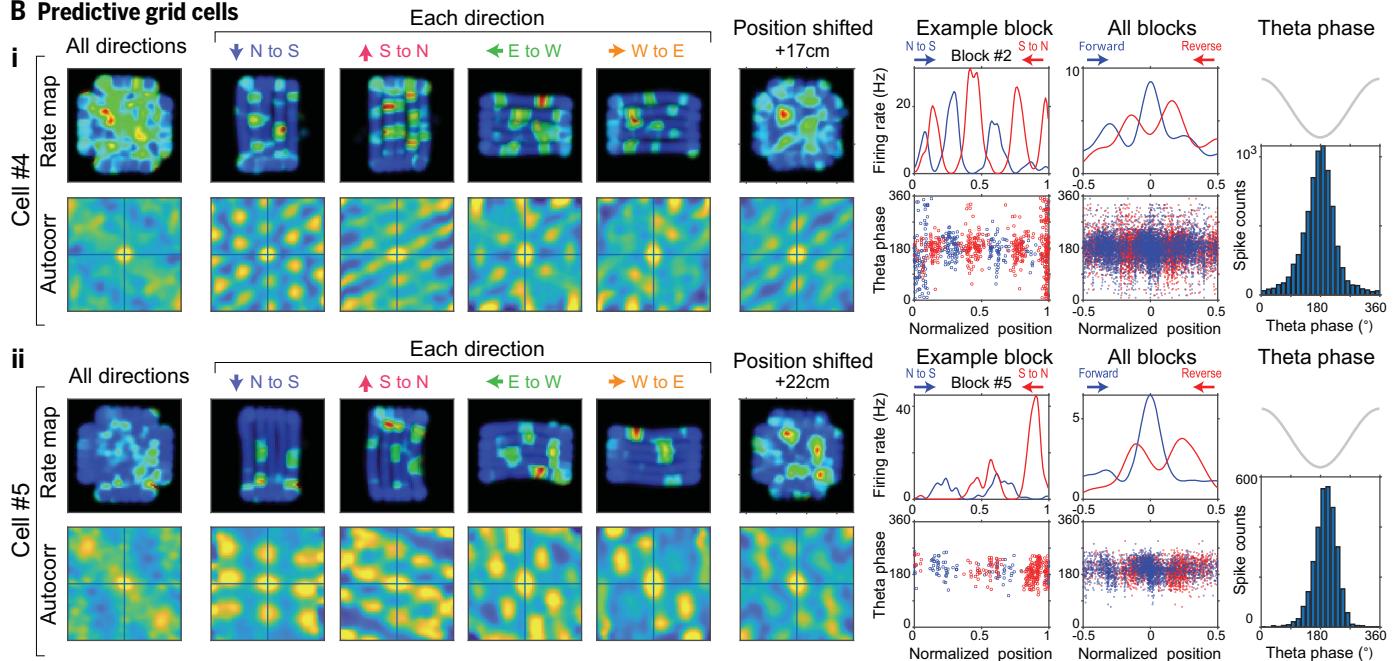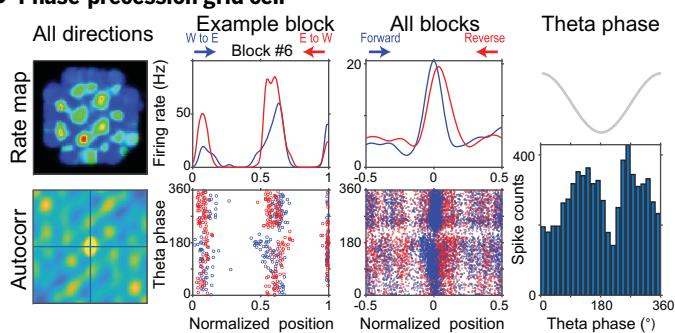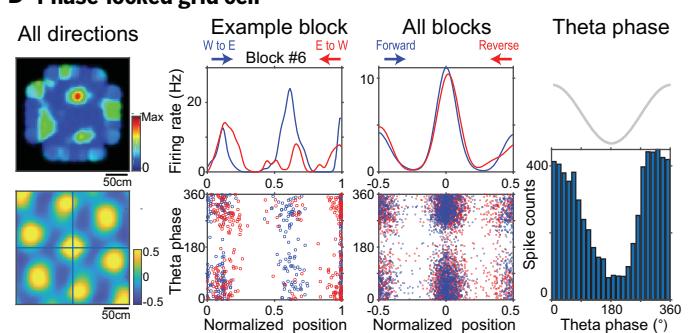
Fig. 1. Predictive grid representations of future spatial information in the MEC. (**A**) Schematic of the task. The rat had to travel back and forth between the two water reward ports in the open field. The positions of the water ports were changed every block to cover the whole environment with vertical, horizontal, and diagonal trajectories. (**B**) The trajectories of a rat in a single session. Each color represents trials of each traveling direction. (**C**) Silicon probes (eight shanks, 16 sites per shank) were placed in the (left) MEC and (right) CA1. Sections with the electrode tracks were stained with Nissl. (**D**) Method for position projection. To construct firing rate maps for the future or past locations, the rat positions were projected forward or backward a fixed length on the trajectory. (**E**) Firing patterns of three representative predictive grid cells in the MEC. (Left) Firing rate maps (top) and their spatial autocorrelations (bottom), whose positional references were original (current position) and future projected. (Middle) Gridness scores as a function of reference positions. A positive position shift indicates a future projection, and a negative shift indicates a past position. (Right) Firing rate modulation by the head direction of the rat. The mean resultant length is shown as r.

phase-locked grid cells, respectively, were significantly correlated with speed (shuffling statistics with preserving positional information) (Fig. 3, I and J). The distributions of head direction modulation of all three types of grid cells were similar (Fig. 3K). The orientations of the grid fields with respect to the arena boundaries of all three types of grid cells were also similar (Fig. 3L) (14). Moreover, we analyzed the anatomical position of all three types of grid cells in the layers of the MEC (fig. S6). Predictive grid cells were mostly located in layer 3 of the MEC. The phase-precession and phase-locked grid cells were distributed in layers 2 and 3, respectively (13).
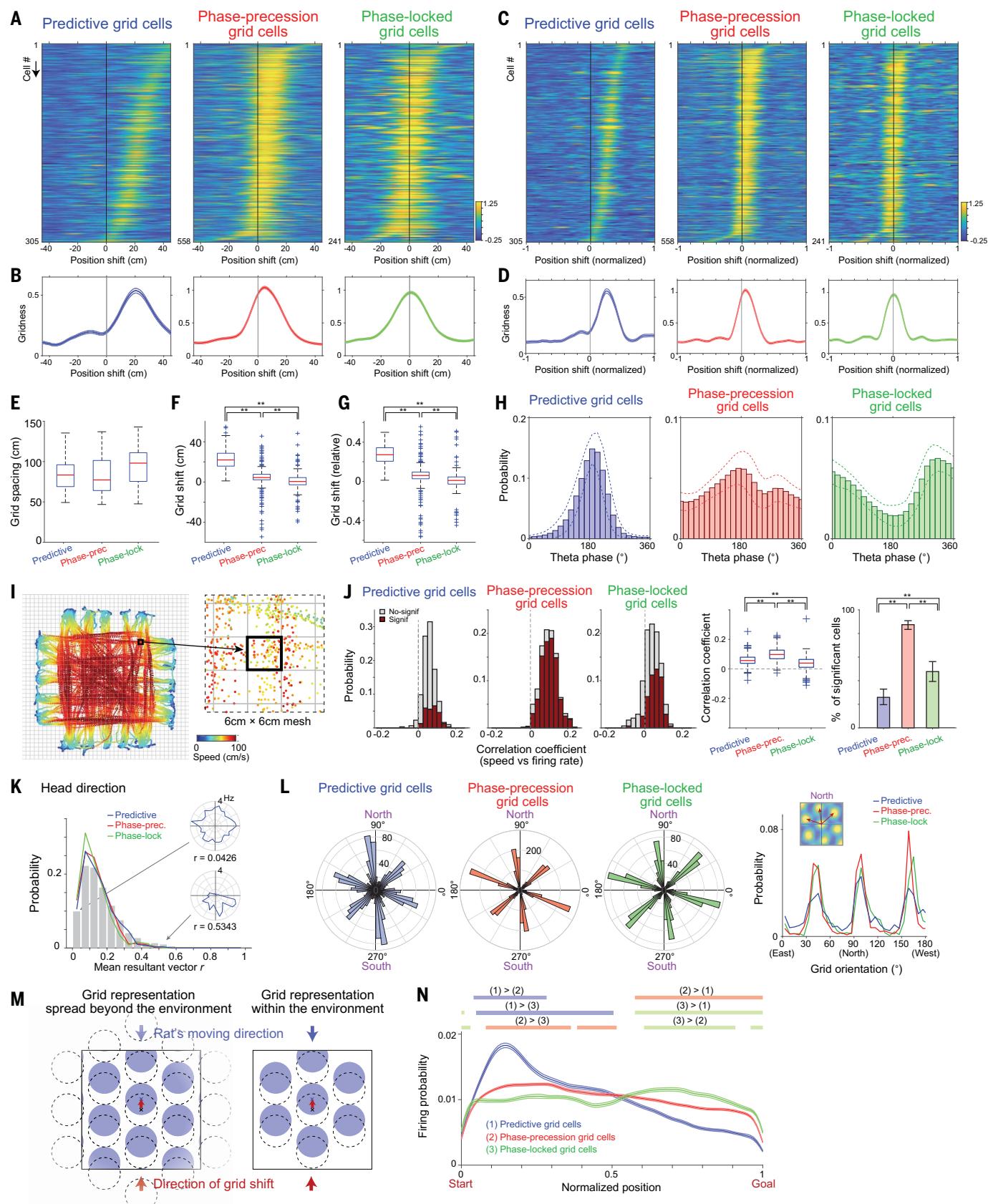
**Fig. 2. Grid fields of predictive grid cells shift in the direction of approach.** (**A**) Model of the spatial representation of predictive grid cells. We hypothesized that the grid fields of predictive grid cells are shifted toward preceding positions in the running trajectory. Because the direction of the shift is different for each traveling direction, the superposition of all directions will cause the grid fields to blur. (**B**) Firing patterns of two predictive grid cells. (Left) Rate maps and spatial autocorrelations of all directions and each direction (north to south, south to north, east to west, and west to east) at original positions, and all directions with future projected positions. (Middle

left) Firing rates and spike phases on theta oscillations in the linearized position in example blocks. (Middle right) Firing rates and spiking theta phases in the linearized position in all blocks (method is provided in fig. S3). (Right) Theta phase preferences of the cells. (**C** and **D**) Firing patterns of a (C) phase-precession grid cell and (D) phase-locked grid cell. (Left) Rate maps and spatial autocorrelations of all directions at the original positions. (Middle left) Firing rates and spike phases in the linearized position in example blocks. (Middle right) Firing rates and spiking phases on theta oscillations in the linearized position in all blocks. (Right) Theta phase preference of the cells.

Fig. 3. Coding properties of predictive, phase-precession, and phase-locked grid cells. (**A**) Gridness scores as a function of position shift of all

predictive, phase-precession, and phase-locked grid cells (n = 305, 558, and 241 cells, respectively, from six rats). (**B**) Mean of the above gridness score plots of

all three types of grid cells. (**C** and **D**) Same as (A) and (B), but the position shift was normalized by the grid spacing. (**E**) Grid spacing of all three types of grid cells. (**F**) Optimal position shift of all three types of grid cells. (**G**) Optimal position shift relative to grid spacing of each cell. **P < 0.001 for (F) and (G); analysis of variance (ANOVA) and post hoc Tukey-Kramer test. (**H**) Average theta phase preferences of all three types of grid cells. (**I**) Speed at the rat's position in the example session. Each dot indicates the position in a 25.6-ms bin, and its color indicates the speed. (**J**) Speed modulations of all three types of grid cells. For the statistical evaluation of the speed tuning, we used the shuffling procedure while preserving the position information (P < 0.01). (Middle) Correlation between speed and firing rate of all three types of grid cells. **P < 0.001; ANOVA and post hoc Tukey-Kramer test. (Right) Proportion of the cells with significant speed modulation for all three types of

grid cells. Clopper-Pearson confidence intervals are shown (**P < 0.01). (**K**) Head direction modulations of all three types of grid cells. Speed modulation of all MEC regular spiking neurons is shown as gray bars. (**L**) Orientation with respect to the arena boundaries of all three types of grid cells in (left) polar and (right) linear plots. (Inset) The orientations of an example cell. (**M**) Models of grid representation for predictive grid cells. (Left) If the grid fields are infinitely distributed, it cannot be distinguished whether the shift of grid fields is in the future or past direction. (Right) If the grid exists only within a finite region enclosed by a boundary, the distribution of the grid field would be different for the future and past shift. (**N**) Overall mean firing rate distribution of predictive, phase-precession, and phase-locked grid cells. The tick lines above the plots indicate the significant period (P < 0.01; permutation tests) (supplementary materials).

We further investigated whether the representation of the predictive grid cells is actually biased toward the future direction (Fig. 3M). For example, if we assume that the grid representation of the predictive grid cells is distributed in the space beyond the task area, we cannot distinguish whether the shift of the grid fields is to the future or to the past. On the other hand, if the grid exists only within a finite region enclosed by a boundary, then the distribution of the grid would be different for future and past shifts. To investigate which model explains the data, we analyzed the distribution of the overall firing rates of predictive grid cells from the start to the goal position. The distribution of mean firing rates of the predictive grid cells was skewed toward the start direction, whereas the distributions of firing rates for phase-precession and phase-locked grid cells were uniform over the whole area (Fig. 3N).

We then examined through which metric the predictive grid cells more strongly reflect the future representation (figs. S7 and S8). In particular, we examined whether predictive grid cells reflect the future in the distance or time domain (*15*). We compared shifting time to shifting locations for computing positional references projecting the future or past (fig. S8). The plots of the gridness scores as a function of the time shift of the predictive grid cells also had the highest peaks in the future time domains, although the peaks of the gridness scores were significantly lower than those of the position shift (fig. S8).

We asked whether predictive coding by predictive grid cells occurs specifically during goal-directed behavior or is broadly general across diverse behaviors. We designed a series of behavioral tasks consisting of goal-directed and random foraging tasks in the same environment (Fig. 4A). We recorded single units from layers 2 and 3 of the MEC and the CA1 during the series of tasks from three other rats. Although there was systematic grid rescaling across the tasks (Fig. 4G) (*16*), the predictive coding properties of the predictive grid cells

were preserved across the goal-directed and random foraging tasks. The results show that the predictive coding of the predictive grid cells is generally present across different behaviors.

Theta sequences in the MEC

Using a Bayesian decoding framework, we tested whether the spikes of the ensembles of predictive, phase-precession, and phase-locked grid cells could reconstruct the rats' future trajectories (*17–20*). The firing rate maps at the optimally shifted position were used as prior templates for these three types of grid cells. We decoded the rat's position from the spiking activity of these neurons in each 10-ms time bin (Fig. 5, A to C). We then examined how the positional information decoded by the spikes of the cell assembly was related to the phases of theta oscillation. The probability densities of the decoded position by using spikes sampled in different theta phases are shown in Fig. 5D. On descending theta phases (0° to 180°), the decoded position progressively reflected more shifted future positions relative to the location at which the spikes were sampled, whereas the decoded position reflected the actual position around peak theta phases (360°) (Fig. 5, D to F). The representation of future positions on the descending theta phases was significantly reduced when the spiking activity of the predictive grid cells was removed for decoding (Fig. 5F). We also examined whether the theta sequence was organized as a result of synchronized activity of cells within the theta cycle or as a result of independent activity of each cell (fig. S9A). The representation of future positions on the descending theta phases was also significantly reduced when the spike synchronization within theta cycles was disrupted (fig. S9).
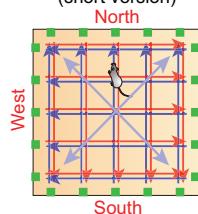
Last, we examined the functional connectivity between the predictive grid cells and CA1 place cells. Predictive grid cells preferred to fire at the trough of theta (180°), whereas CA1 place cells typically exhibit phase precession (*21–23*). Therefore, there may be a relationship between the difference in the firing phases

of predictive grid cells and CA1 place cells and the distance in their spatial receptive fields (fig. S10). To test this, we analyzed the relationship between the location differences in the place (or grid) fields and the firing phase differences for pairs of simultaneously recorded predictive grid cells and CA1 place cells. Synchronous firing activity, as estimated from cross-correlogram (CCG) peaks, occurred when the place fields of predictive grid cells and CA1 place cells overlapped. As expected from the above model, there was a linear relationship between the phase of spiking and the distance between the receptive fields. Significant CCG peaks were observed more frequently when the receptive field of the predictive grid cell was in a preceding position compared with that of the CA1 place cell, suggesting spike transmission from the predictive grid cells to the CA1 place cells, which indicates that the probability of spike transmission from predictive grid cells to CA1 place cells increases when the grid fields of predictive grid cells precede CA1 place fields.
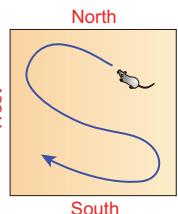
Discussion

We identified a group of MEC neurons with predictive grid coding for their future projected locations. Seeking the coding principle of these predictive grid cells, we found that their grid fields were shifted against the direction of travel. Another distinctive feature of these cells was their robust phase locking to the trough (~180°) of theta oscillations referenced to the CA1 pyramidal cell layers, distinct from phase-precession and phase-locked grid cells, which had different phase preferences. As a result, assemblies of predictive, phase-precession, and phase-locked grid cells in the MEC together temporally organize continuous theta sequences from current to future locations (Fig. 5).
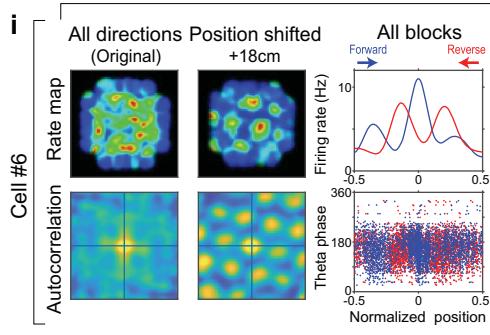
The MEC and hippocampus organize spatial representations to support the awareness of the current position in the environment (*3, 24–26*). Additionally, the spatial representations in the MEC and CA1 encompass not only the current position but also predictive information about
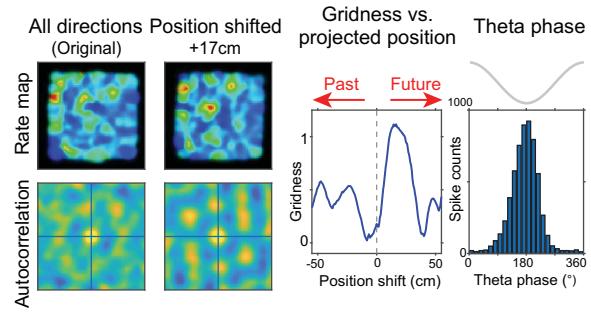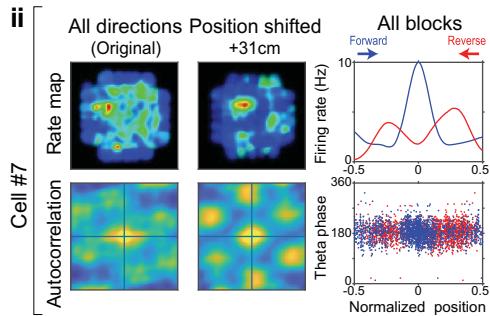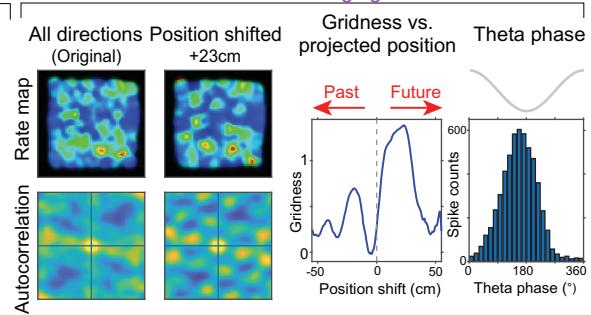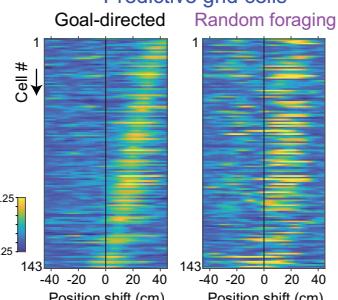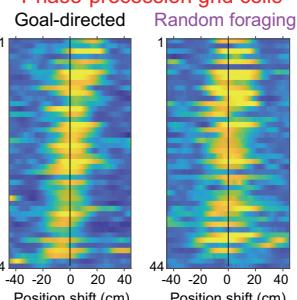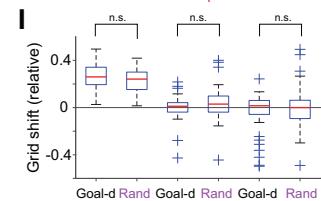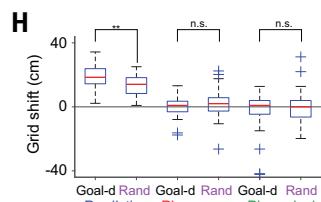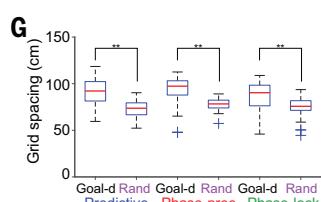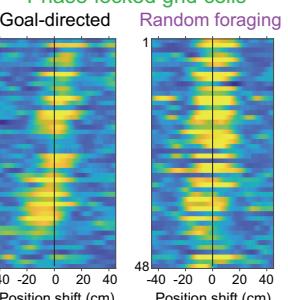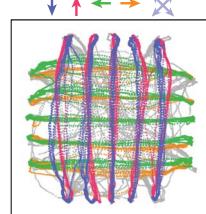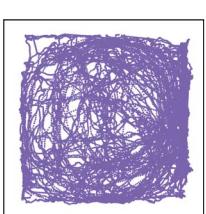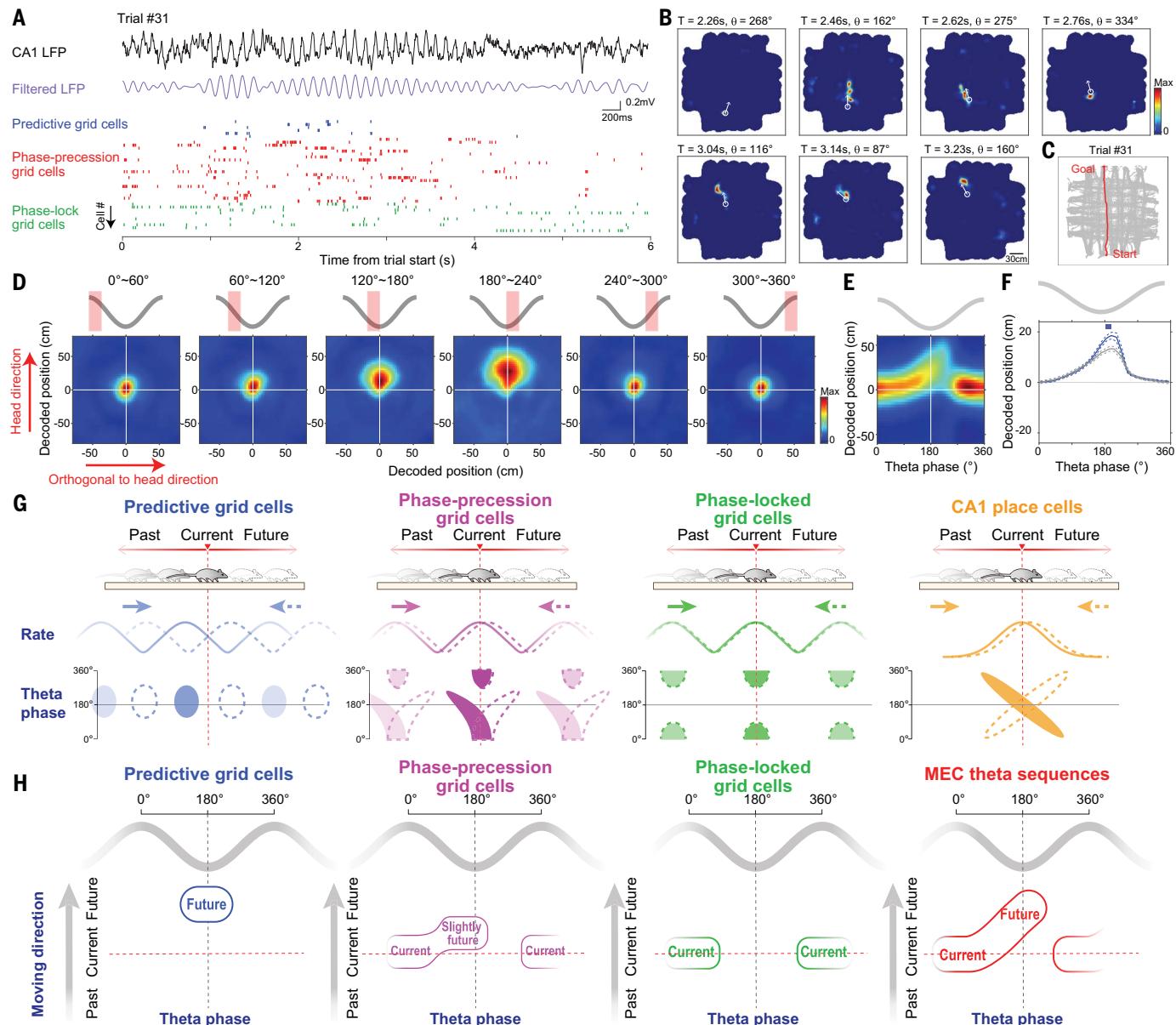
**Fig. 4. Predictive grid coding preserved across different behaviors.**
(**A**) Rats performed a series of goal-directed (short version) and random foraging tasks in the same environment. (**B**) The trajectories of a rat in a single session. (**C**) Firing patterns of two representative predictive grid cells in the goal-directed and random foraging tasks. (Left) Firing rate maps (top) and their spatial autocorrelations (bottom), whose positional references were original and future-projected. (Middle) Gridness scores as a function of reference positions. (**D**) Gridness scores as a function of position shift of all predictive, phase-precession,

and phase-locked grid cells (n = 143, 44, and 48 cells, respectively, from three rats). (**E**) Mean of the above gridness score plots of all three types of grid cells. (**F**) Average theta phase preferences of all three types of grid cells. (**G**) Grid spacing of all three types of grid cells in the two tasks. (**H**) Optimal position shift of all three types of grid cells in the two tasks. (**I**) Optimal position shift relative to the grid spacing of each cell. In the analysis of (G) to (I), neurons that had significant gridness scores at the optimal shift in both tasks were analyzed (n = 53, 42, and 48 cells, respectively). **$P < 0.01$, paired t test.

Fig. 5. Theta sequences for predictive spatial information in the MEC.
(**A**) Raster plots of simultaneously recorded predictive, phase-precession, and phase-locked grid cells in a representative trial. CA1 LFP and its filtered trace with the theta band (4 to 10 Hz) are also shown. (**B**) Probability densities of rat's position at seven example time points, decoded from spiking activities of neurons in (A). The actual locations and head direction of the rats are indicated with white circles and arrows, respectively. Theta phases at the decoded times are also indicated. (**C**) The actual trajectory (red) of the rat in the example trial. (**D**) Two-dimensional probability densities of decoded rat's position in different theta phases in the example session. The decoded positions were aligned with the actual position and head direction of the rat. (**E**) One-dimensional probability densities of position information as a function of theta phases in the example session. The y axis represents decoded positions aligned with the actual position in the axis of the head direction. (**F**) Decoded positional information (the argument of the maximum of probability densities) in the axis of the head direction as a function of theta phases (n = 25 sessions) (supplementary materials). Blue lines indicate the decoding data by using predictive, phase-precession, and phase-locked grid cells, and gray lines indicate those excluding predictive grid cells (mean ± SEM). A thick blue line above the plots indicates a segment with significantly higher values ($P < 0.05$; permutation test). (**G**) Schematic illustration of rate and temporal coding of predictive, phase-precession, and phase-locked grid cells in the MEC and place cells in the CA1. For rate coding, the grid fields of predictive grid cells are shifted to the predictive direction of travel. For temporal coding, predictive grid cells discharge around the troughs of theta oscillations. (**H**) Theta sequences in the MEC. In the peak phases of theta oscillations, phase-precession and phase-locked grid cells encode current positions. In the descending phases, predictive and phase-precession grid cells organize the trajectory sequence representation from current to future positions.

future spatial paths (*27, 28*). Place and grid cells often show a bias toward representing slightly future positions in the path of travel (*15, 29–31*). Moreover, the place and grid cell firing exhibits phase precession, encoding sequences of positions as a function of theta phase (*13, 21, 32, 33*). In the hippocampus, synchronized activity of place cell assemblies organizes theta sequences representing past-to-future trajectories (*22, 23, 34*). However, much remains to be clarified about the relationship between predictive spatial information processing in the axis of the hippocampus and entorhinal cortex (*15*). The predictive grid cells reported here exhibit grid fields specific to the future projected space. We observed and quantified predictive shifts in the grid fields of these cells using the behavioral task consisting of multiple linear tracks in the two-dimensional field. Previous studies that investigated MEC activity in one-dimensional trajectories have also reported the offset or remap of the spatial receptive fields (*32, 35–37*), which is consistent with our findings. Our discovery of predictive grid cells suggests their potential role in supporting the formation of predictive cognitive maps.

We found that the assembly activity of predictive, phase-precession, and phase-locked grid cells organizes the theta sequences that represent trajectories from current to future positions. We hypothesize that predictive grid coding in the MEC may also contribute to the formation of predictive sequences in the hippocampus. In CA1, theta sequences represent past, present, and future trajectories along the early to late phases of the theta oscillations (*22, 23, 34, 38–41*). Several important theories, including the oscillatory interference model (*42, 43*) and the soma-dendrite interference model (*44, 45*), have been proposed as mechanisms for theta phase precession in the CA1 (*18, 46–48*). In addition, the importance of the MEC projection to CA1 as a mechanism of sequence generation has received considerable attention in recent years (*49–53*). The dual input model suggests that the place field activity of CA1 neurons is driven by MEC layer 3 input at theta peaks and associated with gamma bursts in stratum lacunosum-moleculare, followed by increasing CA3 input around the trough of theta phases associated with a gamma increase in stratum radiatum, indicating the fundamental role of the MEC input in generating predictive sequences of CA1 in late theta phases (*52*). The necessity of the MEC in sequence generation is also supported by a recent study showing that optogenetic perturbation of the MEC at gamma frequency abolished predictive theta sequences without affecting associative spatial coding by place cells in the CA1 (*53*). Regarding the theta phase preferences of MEC neurons, it was known that layer 2 neurons exhibit phase precession start-

ing at 180º, and layer 3 neurons are phase-locked at 0º or 180º (*13, 33, 54*). However, it remained unknown how EC neurons convey predictive spatial information to CA1 place cells at the time of late theta phases to support the generation of theta sequences. The predictive grid cells reported here fire at the trough of theta, just before the late theta phases at which CA1 encodes future information. Our data showed a significant increase in functional connectivity between the predictive grid cells and the CA1 place cells when the grid fields of the predictive grid cell preceded the place fields of the CA1 place cells. Predictive grid cells are thus candidates for cells that can provide future information to CA1. Thus, we hypothesize that predictive grid cells in the MEC play a key role in the formation of predictive sequences in the hippocampus.

The mechanism of predictive coding in the predictive grid cells is an open question. We hypothesize that the self-motion information provided by the speed and head direction cells in the MEC may play an essential role (*6, 8*). Theoretical studies have proposed that the input of speed and head direction information into the recurrent network circuits that mode MEC circuit connectivity may generate attractor dynamics with spatial grid structures (*12, 55*). Further investigation of network dynamics in ECs is needed to provide new insights into the mechanism of such predictive coding.

Predictive grid cells provide predictive spatial representations by projecting the grid fields in the approach direction of travel. The predictive, phase-precession, and phase-locked grid cells of the MEC encode current and future information in separate phases of theta oscillations, allowing the formation of theta sequences from current to future locations. We hypothesize that the MEC not only integrates allocentric and egocentric information in spatial navigation but also serves important functions in the integration and prediction of temporal information.

REFERENCES AND NOTES

1. J. O'Keefe, L. Nadel, *The Hippocampus as a Cognitive Map* (Oxford Univ. Press, 1978).
2. T. E. J. Behrens *et al.*, *Neuron* **100**, 490–509 (2018).
3. B. L. McNaughton, F. P. Battaglia, O. Jensen, E. I. Moser, M. B. Moser, *Nat. Rev. Neurosci.* **7**, 663–678 (2006).
4. G. Buzsáki, E. I. Moser, *Nat. Neurosci.* **16**, 130–138 (2013).
5. M. Hafting, M. Fyhn, S. Molden, M. B. Moser, E. I. Moser, *Nature* **436**, 801–806 (2005).
6. F. Sargolini *et al.*, *Science* **312**, 758–762 (2006).
7. T. Solstad, C. N. Boccara, E. Kropff, M. B. Moser, E. I. Moser, *Science* **322**, 1865–1868 (2008).
8. E. Kropff, J. E. Carmichael, M. B. Moser, E. I. Moser, *Nature* **523**, 419–424 (2015).
9. C. Wang *et al.*, *Science* **362**, 945–949 (2018).
10. Ø. A. Høydal, E. R. Skytøen, S. O. Andersson, M. B. Moser, E. I. Moser, *Nature* **568**, 400–404 (2019).
11. R. J. Gardner *et al.*, *Nature* **602**, 123–128 (2022).
12. Y. Burak, I. R. Fiete, *PLOS Comput. Biol.* **5**, e1000291 (2009).
13. T. Hafting, M. Fyhn, T. Bonnevie, M. B. Moser, E. I. Moser, *Nature* **453**, 1248–1252 (2008).
14. J. Krupic, M. Bauza, S. Burton, C. Barry, J. O'Keefe, *Nature* **518**, 232–235 (2015).
15. P. Chaudhuri-Vayalambrone *et al.*, *Cell Rep.* **42**, 112716 (2023).
16. C. Barry, R. Hayman, N. Burgess, K. J. Jeffery, *Nat. Neurosci.* **10**, 682–684 (2007).
17. T. J. Davidson, F. Kloosterman, M. A. Wilson, *Neuron* **63**, 497–507 (2009).
18. T. Feng, D. Silva, D. J. Foster, *J. Neurosci.* **35**, 4890–4902 (2015).
19. S. Terada, Y. Sakurai, H. Nakahara, S. Fujisawa, *Neuron* **94**, 1248–1262.e4 (2017).
20. T. Danjo, T. Toyoizumi, S. Fujisawa, *Science* **359**, 213–218 (2018).
21. J. O'Keefe, M. L. Recce, *Hippocampus* **3**, 317–330 (1993).
22. W. E. Skaggs, B. L. McNaughton, M. A. Wilson, C. A. Barnes, *Hippocampus* **6**, 149–172 (1996).
23. G. Dragoi, G. Buzsáki, *Neuron* **50**, 145–157 (2006).
24. L. Acharya, Z. M. Aghajan, C. Vuong, J. J. Moore, M. R. Mehta, *Cell* **164**, 197–207 (2016).
25. G. Ginosar *et al.*, *Nature* **596**, 404–409 (2021).
26. J. W. Rueckemann, M. Sosa, L. M. Giocomo, E. A. Buffalo, *Nat. Rev. Neurosci.* **22**, 637–649 (2021).
27. L. M. Frank, E. N. Brown, M. Wilson, *Neuron* **27**, 169–178 (2000).
28. K. L. Stachenfeld, M. M. Botvinick, S. J. Gershman, *Nat. Neurosci.* **20**, 1643–1653 (2017).
29. F. P. Battaglia, G. R. Sutherland, B. L. McNaughton, *J. Neurosci.* **24**, 4541–4550 (2004).
30. L. De Almeida, M. Idiart, A. Villavicencio, J. Lisman, *Hippocampus* **22**, 1647–1651 (2012).
31. R. U. Muller, J. L. Kubie, *J. Neurosci.* **9**, 4101–4110 (1989).
32. V. H. Brun *et al.*, *Hippocampus* **18**, 1200–1212 (2008).
33. K. Mizuseki, A. Sirota, E. Pastalkova, G. Buzsáki, *Neuron* **64**, 267–280 (2009).
34. D. J. Foster, M. A. Wilson, *Hippocampus* **17**, 1093–1099 (2007).
35. D. Derdikman *et al.*, *Nat. Neurosci.* **12**, 1325–1332 (2009).
36. J. Nagele, A. V. M. Herz, M. B. Stemmler, *Hippocampus* **30**, 367–383 (2020).
37. M. Pröll, S. Häusler, A. V. M. Herz, *J. Neurosci.* **38**, 7004–7011 (2018).
38. J. R. Huxter, T. J. Senior, K. Allen, J. Csicsvari, *Nat. Neurosci.* **11**, 587–594 (2008).
39. A. M. Wikenheiser, A. D. Redish, *Nat. Neurosci.* **18**, 289–294 (2015).
40. K. Kay *et al.*, *Cell* **180**, 552–567.e25 (2020).
41. S. E. Qasim, I. Fried, J. Jacobs, *Cell* **184**, 3242–3255.e10 (2021).
42. J. O'Keefe, N. Burgess, *Hippocampus* **15**, 853–866 (2005).
43. N. Burgess, *Hippocampus* **18**, 1157–1174 (2008).
44. A. Kamondi, L. Acsády, X. J. Wang, G. Buzsáki, *Hippocampus* **8**, 244–261 (1998).
45. K. D. Harris *et al.*, *Nature* **417**, 738–741 (2002).
46. M. R. Mehta, A. K. Lee, M. A. Wilson, *Nature* **417**, 741–746 (2002).
47. Z. M. Aghajan *et al.*, *Nat. Neurosci.* **18**, 121–128 (2015).
48. S. J. Middleton, T. J. McHugh, *Nat. Neurosci.* **19**, 945–951 (2016).
49. M. I. Schlesiger *et al.*, *Nat. Neurosci.* **18**, 1123–1132 (2015).
50. C. Zheng, K. W. Bieri, Y. T. Hsiao, L. L. Colgin, *Neuron* **89**, 398–408 (2016).
51. N. T. M. Robinson *et al.*, *Neuron* **94**, 677–688.e6 (2017).
52. A. Fernández-Ruiz *et al.*, *Neuron* **93**, 1213–1226.e5 (2017).
53. C. Liu, R. Todorova, W. Tang, A. Oliva, A. Fernandez-Ruiz, *Science* **382**, eadi8237 (2023).
54. L. M. Frank, E. N. Brown, M. A. Wilson, *J. Neurophysiol.* **86**, 2029–2040 (2001).
55. C. Barry, N. Burgess, *Curr. Biol.* **24**, R330–R339 (2014).

SUPPLEMENTARY MATERIALS

science.org/doi/10.1126/science.ado4166
Materials and Methods
Figs. S1 to S10
Table S1
References (56–66)
MDAR Reproducibility Checklist